
Inference for Generative Capsule Models

Alfredo Nazabal^{*†1}

Nikolaos Tsagkas^{*‡2}

Christopher K. I. Williams^{3,4}

¹Amazon Development Centre Scotland, Edinburgh, UK

²tsagkas.nikolas@gmail.com

³School of Informatics, University of Edinburgh, Edinburgh EH8 9AB, UK

⁴The Alan Turing Institute, London, UK

Abstract

Capsule networks (see e.g. Hinton et al., 2018) aim to encode knowledge and reason about the relationship between an object and its parts. In this paper we specify a *generative* model for such data, and derive a variational algorithm for inferring the transformation of each object and the assignments of observed parts to the objects. We apply this model to (i) data generated from multiple geometric objects like squares and triangles (“constellations”), and (ii) data from a parts-based model of faces. Recent work by Kosiorek et al. [2019] has used amortized inference via stacked capsule autoencoders (SCAEs) to tackle this problem—our results show that we significantly outperform them where we can make comparisons (on the constellations data).

1 INTRODUCTION

An attractive way to set up the problem of object recognition is *hierarchically*, where an object is described in terms of its parts, and these parts are in turn composed of sub-parts, and so on. For example a face can be described in terms of the eyes, nose, mouth, hair, etc.; and a teapot can be described in terms of a body, handle, spout and lid parts. This approach has a long history in computer vision, see e.g. Recognition-by-Components by Biederman [1987]. Advantages of recognizing objects by first recognizing their constituent parts include tolerance to the occlusion of some parts, and that parts may vary less under a change of pose than the appearance of the whole object.

One big advantage of a parts-based setup is that if the pose¹ of the object changes, this can have very complicated effects on the pixel intensities in an image, but the geometric transformation between the object and the parts can be described by a simple linear transformation (as used in computer graphics). Convolutional neural networks can allow a recognition system to handle 2D shifts of an object in the image plane, but attempts to generalize such equivariances across more general transformations lead to cumbersome constructions, and have not been very successful.

Recent work by Hinton and collaborators [Sabour et al., 2017, Hinton et al., 2018] has developed *capsule networks*. The key idea here is that a part in a lower level can vote for the pose of an object in the higher level, and an object’s presence is established by the agreement between votes for its pose. Hinton et al. [2018, p. 1] use an iterative process called “routing-by-agreement” which “updates the probability with which a part is assigned to a whole based on the proximity of the vote coming from that part to the votes coming from other parts that are assigned to that whole”. Subsequently Kosiorek et al. [2019] framed inference for a capsule network in terms of an autoencoder, the Stacked Capsule Autoencoder (SCAE). Here, instead of the iterative routing-by-agreement algorithm, a neural network h^{caps} takes as input the set of input parts and outputs predictions for the object capsules’ instantiation parameters $\{\mathbf{y}_k\}_{k=1}^K$. Further networks h_k^{part} are then used to predict part candidates from each \mathbf{y}_k .

The objective function used in Hinton et al. [2018] (their eq. 4) is quite complex (involving four separate terms), and is not derived from first principles. In this paper we argue that the description in the paragraph above is backwards—it is more natural to describe the generative process *by which an object gives rise to its parts*, and that the appropriate routing-by-agreement inference algorithm then falls out naturally from this principled formulation. Below we focus on a single-layer of part-object relations, as we need to show

^{*}Equal contribution.

[†]Work carried out while AN was at the Alan Turing Institute.

[‡]Part of this work was carried out when NT was a MSc student at the University of Edinburgh.

¹i.e. the location and rotation of the object in 2D or 3D.

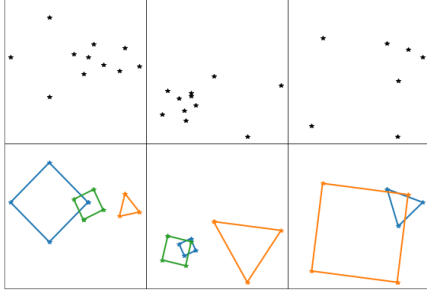


Figure 1: Scenes composed of 2D points (upper figures) and their corresponding objects (lower figures).

first that this is working properly; but the generative model should be readily extensible to deeper hierarchies.

The contributions of this paper are to:

- Derive a variational inference algorithm for a generative model of object-part relationships, including a relaxation of the permutation-matrix formulation for matching object parts to observations;
- Obtain a principled and novel routing-by-agreement algorithm from this formulation;
- Demonstrate the effectiveness of our method on (i) “constellations” data generated from multiple geometric objects (e.g. triangles, squares) at arbitrary translations, rotations and scales; and (ii) data from a novel parts-based model of faces.
- Evaluate the performance of our model vs. competitors on the constellations data.

2 OVERVIEW

Our images consist of a set of objects in different poses. Examples include images of handwritten digits, faces, or geometric shapes in 2D or 3D. An object can be defined as an instantiation of a specific model object (or template) along with a particular pose (or geometric transformation). Furthermore, objects, and thus templates, are decomposed in parts, which are the basic elements that comprise the objects. For example, faces can be decomposed into parts (e.g. mouth, nose etc.), or a geometric shape can be decomposed into vertices. These parts can have internal variability, (e.g. eyes open or shut).

More formally, let $T = \{T_k\}_{k=1}^K$ be the set of K templates that are used to generate a scene. Each template $T_k = \{\mathbf{p}_n\}_{n=1}^{N_k}$ is composed of N_k parts \mathbf{p}_n . We assume that scenes can only be generated using the available templates. Furthermore, every scene can present a different configuration of objects, with some objects missing from some scenes. For example, in scenes that could potentially contain all digits from 0 to 9 once, and if only the digits 2

and 5 are in the image, we consider that the other digits are missing. If all the templates were employed in the scene, then the number of observed parts M is equal to the sum of all the parts of all the templates $N = \sum_{k=1}^K N_k$.

Each observed template T_k in a scene is then transformed by an independent transformation \mathbf{y}_k , different for each template, generating a transformed object $X_k = \{\mathbf{x}_n\}_{n=1}^{N_k}$

$$T_k \xrightarrow{\mathbf{y}_k} X_k. \quad (1)$$

The transformation \mathbf{y}_k includes a geometric transformation of the template, but also includes appearance variability in the parts.

Assume that we are given a scene $X = \{\mathbf{x}_m\}_{m=1}^M$ composed of M observed parts coming from multiple templates. The *inference problem* for X involves a number of different tasks. We need to determine which objects from the set of templates were employed to generate the scene. Also, we need to infer what transformation \mathbf{y}_k was applied to each template to generate the objects. This allows us to infer the *correspondences* between the template parts and the scene parts.

We demonstrate our method on “constellations” data as shown in Fig. 1, and data from a parts-based model of faces illustrated in Fig. 2.

3 GENERATIVE MODEL FOR CAPSULES

We propose a generative model to describe the problem. Consider a template (or model) T_k for the k th object. T_k is composed of N_k parts $\{\mathbf{p}_n\}_{n=1}^{N_k}$.² Each part \mathbf{p}_n is described in its reference frame by its *geometry* \mathbf{p}_n^g and its *appearance* \mathbf{p}_n^a . Each object also has associated latent variables \mathbf{y}_k which transform from the reference frame to the image frame, so \mathbf{y}_k is split into geometric variables \mathbf{y}_k^g and appearance variables \mathbf{y}_k^a .

Geometric transformations: Here we consider 2D templates and a similarity transformation (translation, rotation and scaling) for each object, but this can be readily extended to allow 3D templates and a scene-to-viewer camera transformation. We assume that \mathbf{p}_n^g contains the x and y locations of the part, and also its size s_n and orientation ϕ_n relative to the reference frame.³ The size and orientation are represented as the projected size of the part onto the x any y axes, as this allows us to use linear algebra to express the transformations (see below). Thus $\mathbf{p}_n^g = (p_{nx}^g, p_{ny}^g, s_n \cos \phi_n, s_n \sin \phi_n)^T$.

²For simplicity of notation we suppress the dependence of \mathbf{p}_n on k for now.

³For the constellations data, the size and orientation information is not present, nor are there any appearance features.

Consider a template with parts \mathbf{p}_n^g for $n = 1, \dots, N_k$ that we wish to scale by a factor s , rotate through with a clockwise rotation angle θ and translate by (t_x, t_y) . We obtain a transformed object with geometric observations for the n th part $\mathbf{x}_n^g = (x_{nx}^g, x_{ny}^g, x_{nc}^g, x_{ns}^g)$, where the c and s subscripts denote the projections of the scaled and rotated part onto the x and y axes respectively (c and s are mnemonic for cosine and sine).

For each part in the template, the geometric transformation works as follows:

$$\begin{pmatrix} x_{nx} \\ x_{ny} \\ x_{nc} \\ x_{ns} \end{pmatrix} = \begin{pmatrix} 1 & 0 & p_{nx} & p_{ny} \\ 0 & 1 & p_{ny} & -p_{nx} \\ 0 & 0 & s_n \cos \phi_n & -s_n \sin \phi_n \\ 0 & 0 & s_n \sin \phi_n & s_n \cos \phi_n \end{pmatrix} \begin{pmatrix} t_x \\ t_y \\ s \cos \theta \\ s \sin \theta \end{pmatrix}. \quad (2)$$

Decoding the third equation, we see that $x_{nc} = s_n s \cos \phi_n \cos \theta - s_n s \sin \phi_n \sin \theta = s_n s \cos(\phi_n + \theta)$ using standard trigonometric identities. The x_{ns} equation is derived similarly. We shorten eq. 2 to $\mathbf{x}_n^g = F_{kn}^g \mathbf{y}_k^g$, where \mathbf{y}_k^g is the \mathbb{R}^4 column vector, and $F_{kn}^g \in \mathbb{R}^{4 \times 4}$ is the matrix to its left. Allowing Gaussian observation noise with precision λ we obtain

$$p(\mathbf{x}_n^g | T_k, \mathbf{y}_k^g) \sim N(\mathbf{x}_n^g | F_{kn}^g \mathbf{y}_k^g, \lambda^{-1} I). \quad (3)$$

The prior distribution over similarity transformations \mathbf{y}_k^g is modelled with a \mathbb{R}^4 Gaussian distribution with mean $\boldsymbol{\mu}_0^g$ and covariance matrix D_0^g :

$$p(Y^g) = \prod_{k=1}^K N(\mathbf{y}_k^g | \boldsymbol{\mu}_0^g, D_0^g). \quad (4)$$

Notice that modelling \mathbf{y}_k^g with a Gaussian distribution implies that we are modelling the translation (t_x, t_y) in \mathbb{R}^2 with a Gaussian distribution. If $\boldsymbol{\mu}_0^g = \mathbf{0}$ and $D_0^g = I_4$ then $s^2 = (y_{k3}^g)^2 + (y_{k4}^g)^2$ has a χ_2^2 distribution, and $\theta = \arctan y_{k4}^g / y_{k3}^g$ is uniformly distributed in its range $[-\pi, \pi]$ by symmetry. For more complex linear transformations (e.g. an affine transformation), we need only to increase the dimension of \mathbf{y}_k^g and change the form of F_{kn}^g , but the generative model in (4) would remain the same.

Appearance transformations: The appearance \mathbf{x}_n^a of part n in the image depends on \mathbf{y}_k^a . For our faces data, \mathbf{y}_k^a is a vector latent variable which models the co-variation of the appearance of the parts via a linear (factor analysis) model; see sec. 5.2 for a fuller description. Hence

$$p(\mathbf{x}_n^a | T_k, \mathbf{y}_k) \sim N(\mathbf{x}_n^a | F_{kn}^a \mathbf{y}_k^a + \mathbf{m}_{kn}^a, D_{kn}^a), \quad (5)$$

where F_{kn}^a maps from \mathbf{y}_k^a to the predicted appearance features in the image, D_{kn}^a is a diagonal matrix of variances and \mathbf{m}_{kn}^a allows for the appearance features to have a non-zero mean. The dimensionality of the n th part of the k th template is d_{kn} . The prior for \mathbf{y}_k^a is taken to be a standard

Gaussian, i.e. $N(\mathbf{0}, I)$. Combining (4) and the prior for \mathbf{y}_k^a , we have that $p(\mathbf{y}_k) = N(\boldsymbol{\mu}_0, D_0)$, where $\boldsymbol{\mu}_0$ stacks $\boldsymbol{\mu}_0^g$ and $\mathbf{0}$ from the appearance, and D_0 is a diagonal matrix with blocks D_0^g and I .

Joint distribution: Let $z_{mnk} \in \{0, 1\}$ indicate whether observed part \mathbf{x}_m matches to part n of object k . Every observation m belongs uniquely to a tuple (k, n) , or in other words, a point \mathbf{x}_m belongs uniquely to the part defined by \mathbf{y}_k acting on the template matrix F_{kn} . The opposite is also partially true; every tuple (k, n) belongs uniquely to a point m or it is unassigned if part n of template k is missing in the scene.

The joint distribution of the variables in the model is given by

$$p(X, Y, Z) = p(X|Y, Z)p(Y)p(Z), \quad (6)$$

where $p(X|Y, Z)$ is a Gaussian mixture model explaining how the points in a scene were generated from the templates

$$p(X|Y, Z) = \prod_{m=1}^M \prod_{k=1}^K \prod_{n=1}^{N_k} N(\mathbf{x}_m | F_{kn} \mathbf{y}_k + \mathbf{m}_{kn}, D_{kn})^{z_{mnk}}, \quad (7)$$

where D_{kn} consists of the diagonal matrices $\lambda^{-1} I$ and D_{kn}^a and \mathbf{m}_{kn} consists of a zero vector for the geometric features stacked on top of the mean for the appearance features \mathbf{m}_{kn}^a . Note that F_{kn} has blocks of zeros so that \mathbf{x}_m^g does not depend on \mathbf{y}_k^a , and \mathbf{x}_m^a does not depend on \mathbf{y}_k^g . Note that such a model for a *single object* with geometric features only was developed by Revow et al. [1996].

Annealing parameter: During the fitting of the model to data, it is useful to modify the covariance matrix D_{kn} to $\beta^{-1} D_{kn}$, where β is a parameter < 1 . The effect of this is to inflate the variances in D_{kn} , allowing greater uncertainty in the inferred matches early on in the fitting process, as used, e.g. in Revow et al. [1996]. β is increased according to an annealing schedule during the fitting.

Match distribution $p(Z)$: In a standard Gaussian mixture model, the assignment matrix Z is characterized by a Categorical distribution, where each point \mathbf{x}_m is assigned to one part

$$p(Z) = \prod_{m=1}^M \text{Cat}(\mathbf{z}_m | \boldsymbol{\pi}), \quad (8)$$

with \mathbf{z}_m being a 0/1 vector with only one 1, and $\boldsymbol{\pi}$ being the probability vector for each tuple (k, n) . However, the optimal solution to our problem occurs when each part of a template belongs uniquely to one observed part in a scene. This means that Z should be a permutation matrix, where each point m is assigned to a tuple (k, n) and vice versa. Notice that a permutation matrix is a square matrix, so if $M \leq N$, we add dummy rows to Z , which are assigned to missing points in the scene.

The set of permutation matrices of dimension N is a discrete set containing $N!$ permutation matrices. They can be modelled with a discrete prior over permutation matrices, assigning each matrix Z_i a probability π_i , such as:

$$p_{perm}(Z) = \sum_{i=1}^{N!} \pi_i I[Z = Z_i] \quad (9)$$

with $\sum_{i=1}^{N!} \pi_i = 1$ and $I[Z = Z_i]$ the indicator function, being equal to 1 if $Z = Z_i$ and 0 otherwise.

The number of possible permutation matrices increases as $N!$, which makes exact inference over permutations intractable. An interesting property of $p_{perm}(Z)$ is that its first moment $\mathbb{E}_{p_{perm}}[Z]$ is a doubly-stochastic (DS) matrix, a matrix of elements in $[0, 1]$ whose rows and columns sum to 1. We propose to relax $p_{perm}(Z)$ to a distribution $p_{DS}(Z)$ that is characterized by the doubly-stochastic matrix A with elements a_{mnk} , such that $\mathbb{E}_{p_{DS}}[Z] = A$:

$$p_{DS}(Z) = \prod_{m=1}^N \prod_{k=1}^K \prod_{n=1}^{N_k} a_{mnk}^{z_{mnk}}. \quad (10)$$

A is fully characterized by $(N-1)^2$ elements. In the absence of any prior knowledge of the affinities, a uniform prior over Z with $a_{mnk} = \frac{1}{N}$ can be used. However, note that p_{DS} can also represent a particular permutation matrix Z_i by setting the appropriate entries of A to 0 or 1, and indeed we would expect this to occur during variational inference (see sec. 4) when the model converges to a correct solution.

4 VARIATIONAL INFERENCE

Variational inference for the above model can be derived similarly to the Gaussian Mixture model case [Bishop, 2006, Chapter 10]. The variational distribution under the mean field assumption is given by $q(Z, Y) = q(Z)q(Y)$, where the optimal solutions for $\log q(Z)$ and $\log q(Y)$ under the generative model can be expressed as

$$\log q(Z) \propto \mathbb{E}_{q(Y)}[\log p(X, Y, Z)], \quad (11)$$

$$\log q(Y) \propto \mathbb{E}_{q(Z)}[\log p(X, Y, Z)]. \quad (12)$$

For $q(Z)$ we obtain an expression with the same distribution model as the prior in (10)

$$q(Z) \propto \prod_{m=1}^N \prod_{k=1}^K \prod_{n=1}^{N_k} \rho_{mnk}^{z_{mnk}}, \quad (13)$$

where ρ_{mnk} represents the unnormalized probability of point m being assigned to tuple (k, n) and vice versa. These unnormalized probabilities have a different form depending on whether we are considering a point that appears in the

scene ($m \leq M$)

$$\log \rho_{mnk} = \log a_{mnk} - \frac{1}{2} \log |\beta^{-1} D_{kn}| - \frac{d_{kn}}{2} \log 2\pi - \frac{\beta}{2} \mathbb{E}_{\mathbf{y}_k} [(\mathbf{x}_m - F_{kn} \mathbf{y}_k - \mathbf{m}_{kn})^T D_{kn}^{-1} (\mathbf{x}_m - F_{kn} \mathbf{y}_k - \mathbf{m}_{kn})], \quad (14)$$

or whether we are considering a dummy row of the prior ($m > M$),

$$\log \rho_{mnk} = \log a_{mnk}, \quad (15)$$

When a point is part of the scene (14), and thus $m \leq M$ the update of ρ_{mnk} is similar to the Gaussian mixture model case. However, if a point is not part of the scene (15), and thus $m > M$ then the matrix is not updated and the returned value is the prior a_{mnk} . This specific choice of distribution for both $p_{DS}(Z)$ and $q(Z)$ leads naturally to the addition of dummy rows that are employed to make the matrix ρ square. Now, the normalized distribution $q(Z)$ becomes:

$$q(Z) = \prod_{m=1}^N \prod_{k=1}^K \prod_{n=1}^{N_k} r_{mnk}^{z_{mnk}}, \quad (16)$$

where $\mathbb{E}_{q(Z)}[z_{mnk}] = r_{mnk}$. The elements r_{mnk} of matrix R represent the posterior probability of each point m being uniquely assigned to the part-object tuple (n, k) and vice-versa. This means that R needs to be a DS matrix. This can be achieved by employing the Sinkhorn-Knopp algorithm [Sinkhorn and Knopp, 1967], which updates a square non-negative matrix by normalizing the rows and columns alternately, until the resulting matrix becomes doubly stochastic (see supp. mat. A for more details). The use of the Sinkhorn-Knopp algorithm for approximating matching problems has also been described by Powell and Smith [2019] and Mena et al. [2020], but note that in our case we also need to alternate with inference for $q(Y)$. Furthermore, the optimal solution to the assignment problem occurs when R is a permutation matrix itself. When this happens we exactly recover a discrete posterior (with the same form as (9)) over permutation matrices where one of them has probability one, with the others being zero.

The distribution for $q(Y)$ is a Gaussian with

$$q(Y) = \prod_{k=1}^K N(\mathbf{y}_k | \boldsymbol{\mu}_k, \Lambda_k^{-1}), \quad (17)$$

$$\Lambda_k = D_0^{-1} + \beta \sum_m \sum_n r_{mnk} F_{kn}^T D_{kn}^{-1} F_{kn}, \quad (18)$$

$$\boldsymbol{\mu}_k = \Lambda_k^{-1} \left[D_0 \boldsymbol{\mu}_0 + \beta \sum_m \sum_n r_{mnk} F_{kn}^T D_{kn}^{-1} (\mathbf{x}_m - \mathbf{m}_{kn}) \right], \quad (19)$$

where the updates for both Λ_k and $\boldsymbol{\mu}_k$ depend explicitly on the annealing parameter β and the templates employed

Algorithm 1 Variational Inference

```
1: Initialize  $\beta, \beta_{max}$  and  $R \sim U[0, 1]^{N \times N}, \forall m, n, k$ 
2:  $R = \text{SinkhornKnopp}(R)$ 
3: while not converged do
4:   Update  $\Lambda_k$  (18),  $\forall k$ 
5:   Update  $\mu_k$  (19),  $\forall k$ 
6:   Update  $\log \rho_{mnk}$  (14)(15),  $\forall m, n, k$ 
7:   Update  $R = \text{SinkhornKnopp}(\rho)$ 
8:   if ELBO has converged then
9:     if  $\beta < \beta_{max}$  then
10:      Anneal  $\beta$ 
11:    else
12:      converged = True
return  $R, \{\mu_k, \Lambda_k\}$ 
```

in the model. Note that the prediction from datapoint m to the mean of \mathbf{y}_k is given by $r_{mnk} F_{kn}^T (D_{kn})^{-1} (\mathbf{x}_m - \mathbf{m}_{kn})$, i.e. a weighted sum of the predictions of each part n with weights r_{mnk} . These expressions remain the same when considering a Gaussian mixture prior such as (8).

The expectation term in (14) under the model and evidence lower error bound (ELBO) are given in supp. mat. A. Algorithm 1 summarizes the inference procedure for this model; the alternating updates of $q(Y)$ and $q(Z)$ carry out routing-by-agreement.

4.1 COMPARISON WITH OTHER OBJECTIVE FUNCTIONS

In Hinton et al. [2018] an objective function $cost_k^h$ is defined (their eq. 1) which considers inference for the pose of a higher-level capsule k on pose dimension h . Translating to our notation, $cost_k^h$ combines the votes from each datapoint m as $cost_k^h = \sum_m r_{mk} \ln P_{m|k}^h$, where $P_{m|k}^h$ is a Gaussian, and r_{mk} is the “routing softmax assignment” between m and k . It is interesting to compare this with our equation (19). Firstly, note that the vote of \mathbf{x}_m to part n in object k is given explicitly by $F_{kn}^T \mathbf{x}_m$, i.e. we do not require introduction of an independent voting mechanism, this falls out directly from the inference. Secondly, note that our R must keep track not only of assignments to objects, but also to parts of the objects. In contrast to Hinton et al. [2018], our inference scheme is derived from variational inference on the generative model, rather than introducing an *ad hoc* objective function.

The specialization of the SCAE method of Kosiorek et al. [2019] to constellation data is called the “constellation capsule autoencoder (CCAЕ)” and discussed in their sec. 2.1.

Under their equation 5, we have that

$$p(\mathbf{x}_{1:M}) = \prod_{m=1}^M \sum_{k=1}^K \sum_{n=1}^N \frac{a_k a_{k,n}}{\sum_i a_i \sum_j a_{ij}} N(\mathbf{x}_m | \mu_{k,n}, \lambda_{k,n}), \quad (20)$$

where $a_k \in [0, 1]$ is the presence probability of capsule k , $a_{k,n} \in [0, 1]$ is the conditional probability that a given candidate part n exists, and $\mu_{k,n}$ is the predicted location of part k, n . The a_k s are predicted by the network h^{caps} , while the $a_{k,n}$ s and $\mu_{k,n}$ s are produced by separate networks h_k^{part} for each part k .

We note that (20) provides an autoencoder style reconstructive likelihood for $\mathbf{x}_{1:M}$, as the a ’s and μ ’s depend on the data. To handle the arbitrary number of datapoints M , the network h^{caps} employs a Set Transformer architecture [Lee et al., 2019]. In comparison to our iterative variational inference, the CCAE is a “one shot” inference mechanism. This may be seen as an advantage, but in scenes with overlapping objects, humans may perform reasoning like “if that point is one of the vertices of a square, then this other point needs to be explained by a different object” etc, and it may be rather optimistic to believe this can be done in a simple forward pass. Also, CCAE cannot exploit prior knowledge of the geometry of the objects, as it relies on an opaque network h^{caps} which requires extensive training.

4.2 RELATED WORK

Above we have discussed the work of Sabour et al. [2017], Hinton et al. [2018] and Kosiorek et al. [2019]. There is some more recent work, for example Li et al. [2020] present an undirected model, based on the capsule RBM of Li and Zhu [2019]. Compared to our work, this is an undirected as opposed to directed generative model. Also Smith et al. [2021] propose a layered directed generative model, where the children of higher level capsules inherit its pose (but transformed). Both Li et al. [2020] and Smith et al. [2021] consider tree-structured relationships between parents and children, similar to Hinton et al. [2000] and Storkey and Williams [2003]. However, most importantly, these recent capsule models do not properly handle the fact that the input to a capsule should be a *set* of parts; instead in their work the first layer capsules that interact with the input image model specific location-dependent features/templates in the image, and their second layer capsules have interactions with the specific first layer capsules (e.g. the fixed affinity ρ_{ij}^k of Smith et al. [2021] parent i in layer k for child j). But if we consider a second-layer capsule that is, for example, detecting the conjunction of the 3 strokes comprising a letter “A”, then at different translations, scales and rotations of the A it will need to connect to different image level stroke features, so these connection affinities must depend on transformation variables of the parent.

4.3 A RANSAC APPROACH TO INFERENCE

A radical alternative to “routing by agreement” inference is to make use of a “random sample consensus” approach (RANSAC, Fischler and Bolles, 1981), where a minimal number of parts are used in order to instantiate an object. The original RANSAC fitted just one object, but Sequential RANSAC (see, e.g., Torr 1998, Vincent and Laganière 2001) repeatedly removes the parts associated with a detected object and re-runs RANSAC, so as to detect all objects.

For the constellations problem, we can try matching any pair of points on one of the templates to every possible pair of $M(M - 1)$ points in the scene. The key insight is that a pair of known points is sufficient to compute the 4-dimensional \mathbf{y}_k vector in the case of similarity transformations. Using the transformation $\hat{\mathbf{y}}_k$, we can then *predict* the location of the remaining parts of the template, and *check* if these are actually present. If so, this provides evidence for the existence of T_k and $\hat{\mathbf{y}}_k$. After considering the $M(M - 1)$ subsets, the algorithm then combines the identified instantiations to give an overall explanation of the scene. Details of RANSAC for the constellations problem are given in supp. mat. B.

For the faces data, each part has location, scale and orientation information, so a single part is sufficient to instantiate the whole object geometrically. For the appearance, we follow the procedure for inference in a factor analysis model with missing data, as given in Williams et al. [2019], to predict \mathbf{y}_k^a given the appearance of the single part.

5 EXPERIMENTAL DETAILS

Below we provide details of the data generators, inference methods and evaluation criteria for the constellations data in sec. 5.1, and the faces data in sec. 5.2.

5.1 CONSTELLATION DATA

In order to allow fair comparisons, we use the same dataset generator for geometric shapes employed by Kosiorek et al. [2019]. We create a dataset of scenes, where each scene consists of a set of 2D points, generated from different geometric shapes. The possible geometric shapes (templates) are a square and an isosceles triangle, with parts being represented by the 2D coordinates of the vertices. We use the same dimensions for the templates as used by Kosiorek et al. [2019], side 2 for the square, and base and height 2 for the triangle. All templates are centered at $(0, 0)$. In every scene there are at most two squares and one triangle. Each shape is transformed with a random transformation to create a scene of 2D points given by the object parts. To match the evaluation of Kosiorek et al. [2019], all scenes are normalized so as the points lie in $[-1, 1]$ on both dimensions. When creating the scene, we select randomly (with probability 0.5)

whether an object is going to be present or not, but delete empty scenes. A test set used for evaluation is comprised of 450-460 non-empty scenes, based on 512 draws.

Additionally, we study how the methods compare when objects are created from noisy templates. We consider that the original templates used for the creation of the images are corrupted with Gaussian noise with standard deviation σ . Once the templates are corrupted with noise, a random transformation \mathbf{y}_k is applied to obtain the object X_k of the scene. As with the noise-free data, the objects are normalized to lie in $[-1, 1]$ on both dimensions.

CCAIE is trained by creating random batches of 128 scenes as described above and optimizing the objective function in (20). The authors run CCAIE for 300K epochs, and when the parameters of the neural networks are trained, they use their model on the test dataset to generate an estimation of which points belong to which capsule, and where the estimated points are located in each scene.

The variational inference approach allows us to model scenes where the points are corrupted with some noise. The annealing parameter β controls the level of noise allowed in the model. We use an annealing strategy to fit β , increasing it every time the ELBO has converged, up to a maximum value of $\beta_{max} = 1$. We set the hyperparameters of the model to $\boldsymbol{\mu}_0^g = \mathbf{0}$, $D_0^g = I_4$, $\lambda = 10^4$ and $a_{mnk} = \frac{1}{N}$. We run Algorithm 1 with 5 different random initializations of R and select the solution with the best ELBO. Similarly to Kosiorek et al. [2019], we incorporate a sparsity constraint in our model, that forces every object to explain at least two parts. Once our algorithm has converged, for a given k if any $r_{mnk} > 0.9$ and $\sum_m \sum_n r_{mnk} < 2$ it means that the model has converged to a solution where object k is assigned to less than 2 parts. In these cases, we re-run Algorithm 1 with a new initialization of R . Notice that this is also related to the minimum basis size necessary in the RANSAC approach for the types of transformations that we are considering.

The implementation RANSAC (Algorithm 3) considers all matches between the predicted and the scene points where the distance between them is less than 0.1. Among them, it selects the matching with minimum distance between scene and predicted points. For both the variational inference algorithm and the RANSAC algorithm, a training dataset is not necessary. These algorithms are applied directly to each test scene and return a set of objects describing the points in the scene. Unfortunately we do not have access to the code employed by Hinton et al. [2018], so we have been unable to make comparisons with it.

Evaluation: Three metrics are used to evaluate the performance of the different methods: variation of information, adjusted Rand index and segmentation accuracy. They are based on partitions of the datapoints into those associated with each object, and those that are missing. Compared



Figure 2: (a) A synthetic face. The red lines indicate the areas of the 5 part types (i.e. hair, eyes, nose, mouth and jaw). (b) Example scene with 3 randomly transformed faces.

to standard clustering evaluation metrics, some modifications are needed to handle the missing objects. Details are provided in supp. mat. C. We also use an average scene accuracy metric, where a scene is correct if the method returns the full original scene, and is incorrect otherwise.

5.2 PARTS-BASED FACE MODEL

We have developed a novel hierarchical parts-based model for face appearances. It is based on five parts, namely eyes, nose, mouth, hair and forehead, and jaw (see Fig. 2(a)). Each part has a specified mask, and we have cropped the hair region to exclude highly variable hairstyles. This decomposition is based on the "PhotoFit Me" work and data of Prof. Graham Pike, see <https://www.open.edu/openlearn/PhotoFitMe>. For each part we trained a probabilistic PCA (PPCA) model to reduce the dimensionality of the raw pixels; the dimensionality is chosen so as to explain 95% of the variance. This resulted in dimensionalities of 24, 11, 12, 16 and 28 for the eyes, nose, mouth, jaw and hair parts respectively. We then add a factor analysis (FA) model on top with latent variables \mathbf{y}_k^a to model the correlations of the PPCA coefficients across parts. The dataset used (from PhotoFit Me) is balanced by gender (female/male) and by race (Black/Asian/Caucasian), hence the high-level factor analyser can model regularities across the parts, e.g. wrt skin tone. \mathbf{x}_n^a is predicted from \mathbf{y}_k^a as $F_{kn}^a \mathbf{y}_k^a + \mathbf{m}_{kn}^a$ as in (5). \mathbf{y}_k^a would have an effect on the part appearance, e.g. by scaling and rotation, but this can be removed by running the PPCA part detectors on copies of the input image that have been rescaled and rotated.

The "PhotoFit Me" project utilizes 7 different part-images for each gender/race group, for each of the five part types. As a result, we generated 7^5 synthetic faces for each group, by combining these face-parts, which led to a total of 100,842 faces. All faces were centered on a 224×224 pixel canvas. For each synthetic face we created an appearance vector \mathbf{x}_n^a , which consisted of the stacked vectors from the 5 dif-

ferent principal component subspaces. Finally, we created a balanced subset from the generated faces (18,000 images), which we used to train a FA model. We tuned the latent dimension of this model by training it multiple times with a different number of factors, and finally chose 12 factors, where a knee in the reconstruction loss on the face data was observed on a validation set.

Early work on PCA for faces—"eigenfaces" [Sirovich and Kirby, 1987, Turk and Pentland, 1991]—used a global basis as opposed to a parts-based representation. Rao and Ballard [1999] made use of a hierarchical factor analysis model, but used it to model extended edges in natural image patches rather than facial parts. Ross and Zemel [2006] developed a "multiple cause factor analysis" (MCFA) and applied it to faces; in contrast to our work this did not have a higher-level factor analyser to model correlations between parts, but it did allow variability in the masks of the parts.

Kosiorok et al. [2019] developed a Part Capsule Autoencoder (PCAE) to learn parts from images, and applied it to MNIST images. Each PCAE part is a template which can undergo an affine transformation, and it has "special features" that were used to encode the colour of the part. Thus the PCAE parts are less flexible than our facial parts—they only model global colour changes of the part, and not the rich variability that can be encoded with the PCA model. Also, we have found that the parts detected by PCAE are not equivariant to rotation. Figure 7 shows the PCAE part decompositions inferred for different angles of rotation of a 4 digit—notice e.g. in panel (a) how the part coloured white maps to different parts of the 4 for 45° - 180° and 225° - 0° .

To evaluate our inference algorithm we generated 224×224 pixel scenes of faces. These consisted of 2, 3, 4 or 5 randomly selected faces from a balanced test-set of 7,614 synthetic faces, which were transformed with random similarity transformations. The face-objects were randomly scaled down by a minimum of 50% and were also randomly translated and rotated, with the constraint that all the faces fit the scene and did not overlap each other. An example of such a scene is shown in Fig. 2(b), and further examples are shown in the supp. mat. Figure 8. Afterwards, these two constraints were dropped to test the ability of our model to perform inference with occluded parts, see Figure 8(e) for an example. In our experiments we assume that the face parts are detected accurately, i.e. as generated.

In the case of facial parts—and parts with both geometric and appearance features in general—it only makes sense to assign the observed parts \mathbf{x}_m to template parts \mathbf{x}_{kn} of the same type (e.g. an observed "nose" part should be assigned only to a template "nose" part). We assume that this information is known, since the size of the appearance vector of each part-type is unique. Thus it no longer makes sense to initialize the assignment matrix uniformly for all entries, but rather only for the entries that correspond to templates of the

Table 1: Comparison between the different methods. For SA, ARI and Scene Accuracy the higher the better. For VI the lower the better. Different levels of Gaussian noise with standard deviation σ are considered.

Metric	Model	$\sigma=0$	$\sigma=0.1$	$\sigma=0.25$
SA \uparrow	CCAЕ	0.828	0.754	0.623
	GCM-GMM	0.753	0.757	0.744
	GCM-DS	0.899	0.882	0.785
	RANSAC	1	0.992	0.965
ARI \uparrow	CCAЕ	0.599	0.484	0.248
	GCM-GMM	0.586	0.572	0.447
	GCM-DS	0.740	0.699	0.498
	RANSAC	1	0.979	0.914
VI \downarrow	CCAЕ	0.481	0.689	0.988
	GCM-GMM	0.478	0.502	0.677
	GCM-DS	0.299	0.359	0.659
	RANSAC	0	0.034	0.135
Scene Acc \uparrow	CCAЕ	0.365	0.138	0.033
	GCM-GMM	0.179	0.173	0.132
	GCM-DS	0.664	0.603	0.377
	RANSAC	1	0.961	0.843

observed part’s type. Consequently, (14) is only utilized for m, n pairs of the same type. Similarly to the constellation experiments, we initialized the assignment matrix 5 times and selected the solution with the largest ELBO.

In the experiments we evaluated the part assignment accuracy of the algorithms. In a given scene, the assignment is considered correct if all the observed parts have been correctly assigned to their corresponding template parts with the highest probability. In order to evaluate the prediction of the appearance features, we measured the root mean square error (RMSE) between the input and generated scenes.

6 RESULTS

We present results for the constellations and faces experiments in sections 6.1 and 6.2 respectively.

6.1 CONSTELLATION EXPERIMENTS

In Table 1 we show a comparison between CCAE, the variational inference method with a Gaussian mixture prior (8) (GCM-GMM), with a prior over permutation matrices (9) (GCM-DS), and the RANSAC approach ⁴. For GCM-GMM and GCM-DS we show the results where the initial $\beta = 0.05$, relegating a comparison across different initializations of β to the supp. mat. E and F. Scenes without noise and with noise levels of $\sigma = 0.1, 0.25$ are considered.

We see that GCM-DS improves over CCAE and GCM-

GMM in all of the metrics, with GCM-GMM being comparable to CCAE. Interestingly, for the noise-free scenarios, the RANSAC method achieves a perfect score for all of the metrics. Since there is no noise on the observations and the method searches over all possible solutions of \mathbf{y}_k , it can find the correct solution for any configuration of geometric shapes in a scene. For the noisy scenarios, all the methods degrade as σ increases. However, the relative performance between them remains the same, with RANSAC performing the best, followed by GCM-DS and then GCM-GMM. Example inferences are shown and discussed in supp. mat. G and H.

6.2 FACE EXPERIMENTS

Firstly, the VI algorithm was evaluated on scenes of multiple, randomly selected and transformed faces ⁵. For scenes with 2, 3, 4 and 5 faces, the assignment accuracy was 100%, 100%, 99.2% and 93.7% respectively (based on 250 scenes per experiment). RANSAC gave 100% accurate assignments in all 4 cases. This is to be expected, since from each part the pose of the whole can be predicted accurately. However, RANSAC’s ability to infer the appearance of the faces proved to be limited. More specifically, in 250 instances uniformly distributed across scenes of 2, 3, 4 and 5 faces, the VI algorithm had RMSE of 0.036 ± 0.004 , while RANSAC scored 0.052 ± 0.006 , with consistently higher error on *all* scenes. This is illustrated in the examples of Figure 8, where it is clear that RANSAC is less accurate in capturing key facial characteristics. If inference for \mathbf{y}_k^a is run as a post-processing step for RANSAC using all detected parts in an object, this difference disappears.

The supp. mat. contains a movie showing the fitting of the models to the data. It is not possible for us to compare results with the SCAE algorithm on the faces data, as the PCAE model used is not rich enough to model PCA subspaces.

Secondly, we evaluated the ability of our algorithm to perform inference in scenes where some parts have been occluded, either by overlapping with other faces or by extending out of the scene. In 250 scenes with 3 partially occluded faces, both the VI and RANSAC algorithms were fully successful in assigning the observed parts to the corresponding template accurately. See Figure 8(e) for an example.

7 DISCUSSION

Above we have described a principled generative capsules model. It leads directly to a variational inference algorithm which can handle either a mixture formulation or incorporation of the DS matrix constraint. We have also shown that this formulation outperforms the CCAE of Kosiorek et al. [2019] on the constellation data generator that they used.

⁴Code at: <https://github.com/anazabal/GenerativeCapsules>

⁵Code at: <https://github.com/tsagakas/capsules>

In our experiments RANSAC was shown to often be an effective alternative to variational inference (VI). This is particularly the case when the basis in RANSAC is highly informative about the object. RANSAC provides an interesting alternative to routing-by-agreement, although its sampling-based inference is less amenable to neural-network style parallel implementations than VI.

In this paper we have not discussed the learning of the geometric model (i.e. the F_{kn}^g matrices), but in all such work, inference for $q(Z, Y)$ forms an inner loop, with model learning as an outer loop. Also, the interpretable nature of the model means that we can exploit knowledge where it is available; in contrast the SCAE's opaque inference networks do not allow this.

Acknowledgements

This work was supported in part by The Alan Turing Institute under EPSRC grant EP/N510129/1.

References

- I. Biederman. Recognition-by-components: A theory of human image understanding. *Psychological Review*, 94: 115–147, 1987.
- C. M. Bishop. *Pattern Recognition and Machine Learning*. Springer, 2006.
- M. A. Fischler and R. C. Bolles. Random sample consensus: a paradigm for model fitting with applications to image analysis and automated cartography. *Communications of the ACM*, 24(6):381–395, 1981.
- G. E. Hinton, Z. Ghahramani, and Y. W. Teh. Learning to Parse Images. In S. A. Solla, T. K. Leen, and K.-R. Müller, editors, *Advances in Neural Information Processing Systems 12*, pages 463–469. MIT Press, Cambridge, MA, 2000.
- G. E. Hinton, S. Sabour, and N. Frosst. Matrix capsules with EM routing. In *International Conference on Learning Representations*, 2018.
- L. Hubert and P. Arabie. Comparing partitions. *Journal of Classification*, 2(1):193–218, 1985.
- A. Kosiorek, S. Sabour, Y. W. Teh, and G. E. Hinton. Stacked capsule autoencoders. In *Advances in Neural Information Processing Systems*, pages 15512–15522, 2019.
- J. Lee, Y. Lee, J. Kim, A. R. Kosiorek, S. Choi, and Y.-W. Teh. Set Transformer: A Framework for Attention-based Permutation-invariant Neural Networks. In *Proc. of the 36th International Conference on Machine Learning*, pages 3744–3753, 2019.
- Y. Li and X. Zhu. Capsule Generative Models. In I. V. Tetko et al., editors, *ICANN*, pages 281–295. LNCS 11727, 2019.
- Y. Li, X. Zhu, R. Naud, and P. Xi. Capsule Deep Generative Model That Forms Parse Trees. In *2020 International Joint Conference on Neural Networks (IJCNN)*. IEEE, 2020.
- M. Meilă. Comparing clusterings by the variation of information. In *Learning Theory and Kernel Machines*, pages 173–187. Springer, 2003.
- Gonzalo Mena, Erdem Varol, Amin Nejatbakhsh, Eviatar Yemini, and Liam Paninski. Sinkhorn permutation variational marginal inference. In *Symposium on Advances in Approximate Bayesian Inference*, pages 1–9. PMLR, 2020.
- B. Powell and P. A. Smith. Computing expectations and marginal likelihoods for permutations. *Computational Statistics*, pages 1–21, 2019.
- W. M. Rand. Objective criteria for the evaluation of clustering methods. *Journal of the American Statistical Association*, 66(336):846–850, 1971.
- R. P. N. Rao and D. H. Ballard. Predictive coding in the visual cortex: a functional interpretation of some extraclassical receptive-field effects. *Nature Neurosci.*, 2(1): 79–87, 1999.
- M. Revow, C. K. I. Williams, and G. E. Hinton. Using Generative Models for Handwritten Digit Recognition. *IEEE Trans. on Pattern Analysis and Machine Intelligence*, 18(6):592–606, 1996.
- D. Ross and R. Zemel. Learning parts-based representations of data. *Journal of Machine Learning Research*, 7:2369–2397, 2006.
- S. Sabour, N. Frosst, and G.E. Hinton. Dynamic routing between capsules. In *Advances in Neural Information Processing Systems*, pages 3856–3866, 2017.
- R. Sinkhorn and P. Knopp. Concerning nonnegative matrices and doubly stochastic matrices. *Pacific Journal of Mathematics*, 21(2):343–348, 1967.
- L. Sirovich and M. Kirby. Low-dimensional Procedure for the Characterization of Human Faces. *Journal of the Optical Society of America A*, 4(3):519–524, 1987.
- L. Smith, L. Schut, Y. Gal, and M. van der Wilk. Capsule Networks—A Generative Probabilistic Perspective, 2021. <https://arxiv.org/pdf/2004.03553.pdf>.
- A. J. Storkey and C. K. I. Williams. Image Modelling with Position-Encoding Dynamic Trees. *IEEE Trans Pattern Analysis and Machine Intelligence*, 25(7):859–871, 2003.

- P. H. S. Torr. Geometric Motion Segmentation and Model Selection. *Philosophical Trans. of the Royal Society A*, 356:1321–1340, 1998.
- M. Turk and A. Pentland. Eigenfaces for Recognition. *Journal of Cognitive Neuroscience*, 3(1):71–86, 1991.
- E. Vincent and R. Laganière. Detecting planar homographies in an image pair. In *Proceedings of the 2nd International Symposium on Image and Signal Processing and Analysis (ISPA)*, 2001.
- C. K. I. Williams, C. Nash, and A. Nazabal. Autoencoders and Probabilistic Inference with Missing Data: An Exact Solution for The Factor Analysis Case, 2019. arXiv:1801.03851.
- H. J. Wolfson and I. Rigoutsos. Geometric hashing: An overview. *IEEE Computational Science and Engineering*, 4(4):10–21, 1997.

Supplementary Material for Inference for Generative Capsule Models

A DETAILS FOR VARIATIONAL INFERENCE

The Sinkhorn-Knopp algorithm is given in Algorithm 2.

Algorithm 2 Sinkhorn-Knopp algorithm

```

1: procedure SINKHORNKNOPP( $X$ )
2:   while  $X$  not doubly stochastic do
3:     Normalize rows of  $X$ :  $x_{ij} = \frac{x_{ij}}{\sum_j x_{ij}}, \forall i$ 
4:     Normalize columns of  $X$ :  $x_{ij} = \frac{x_{ij}}{\sum_i x_{ij}}, \forall j$ 
   return  $X$ 

```

The evidence lower bound (ELBO) $L(q)$ for this model is decomposed in three terms:

$$L(q) = \mathbb{E}_q[\log p(X|Y, Z)] - KL(q(Y)||p(Y)) - KL(q(Z)||p(Z)), \quad (21)$$

with $KL(q||p)$ being the Kullback-Leibler divergence between distributions q and p . The first term indicates how well the generative model $p(X|Y, Z)$ fits the observations under our variational model $q(Y, Z)$:

$$\begin{aligned} \mathbb{E}_q[\log p(X|Y, Z)] = & - \sum_{m=1}^M \sum_{k=1}^K \sum_{n=1}^{N_k} r_{mnk} \left[\frac{d_{kn}}{2} \log 2\pi + \frac{1}{2} \log |\beta^{-1} D_{kn}| \right. \\ & + (\mathbf{x}_m - F_{kn}\boldsymbol{\mu}_k - \mathbf{m}_{kn})^T D_{kn}^{-1} (\mathbf{x}_m - F_{kn}\boldsymbol{\mu}_k - \mathbf{m}_{kn}) \\ & \left. + \text{trace}(F_{kn}^T D_{kn}^{-1} F_{kn} \Lambda_k^{-1}) \right]. \quad (22) \end{aligned}$$

The Kullback-Leibler divergence between the two Gaussian distributions $q(Y)$ and $p(Y)$ in our model has the following expression:

$$\begin{aligned} KL(q(Y)||p(Y)) = & \frac{1}{2} \sum_{k=1}^K (\text{trace}(D_0^{-1} \Lambda_k^{-1}) - d_k + \\ & (\boldsymbol{\mu}_k - \boldsymbol{\mu}_0)^T D_0^{-1} (\boldsymbol{\mu}_k - \boldsymbol{\mu}_0) + \log |D_0| + \log |\Lambda_k|), \quad (23) \end{aligned}$$

where d_k is the dimensionality of \mathbf{y}_k .

The expression for $KL(q(Z)||p(Z))$ is given by

$$KL(q(Z)||p(Z)) = \sum_{m=1}^N \sum_{k=1}^K \sum_{n=1}^{N_k} r_{mnk} \log \frac{r_{mnk}}{a_{mnk}}. \quad (24)$$

Algorithm 3 RANSAC approach

```

1:  $T$ :  $K$  templates of the scene
2:  $B_k$ : base matrix for template  $T_k$ 
3:  $X$ :  $M$  points of the scene
4:  $out = []$ 
5: for  $\mathbf{x}_i \in X$  do
6:   for  $\mathbf{x}_j \in X \setminus \mathbf{x}_i$  do
7:      $\mathbf{x}_{ij} = \text{Vectorize}(\mathbf{x}_i, \mathbf{x}_j)$ 
8:     for  $k = 1 : K$  do
9:        $\hat{\mathbf{y}}_k = B_k^{-1} \mathbf{x}_{ij}$ 
10:       $T_k \xrightarrow{\hat{\mathbf{y}}_k} \hat{X}_k$ 
11:      if  $\text{SubsetMatch}(\hat{X}_k, X)$  then
12:        Add  $(T_k, \hat{\mathbf{y}}_k, \hat{X}_k)$  to  $out$ 
   return  $out$ 

```

The expectation term in (14) is:

$$\begin{aligned} \mathbb{E}_{\mathbf{y}_k}[(\mathbf{x}_m - F_{kn}\mathbf{y}_k - \mathbf{m}_{kn})^T D_{kn}^{-1} (\mathbf{x}_m - F_{kn}\mathbf{y}_k - \mathbf{m}_{kn})] \\ = (\mathbf{x}_m - F_{kn}\boldsymbol{\mu}_k - \mathbf{m}_{kn})^T D_{kn}^{-1} (\mathbf{x}_m - F_{kn}\boldsymbol{\mu}_k - \mathbf{m}_{kn}) \\ + \text{trace}(F_{kn}^T D_{kn}^{-1} F_{kn} \Lambda_k^{-1}). \quad (25) \end{aligned}$$

B DETAILS OF RANSAC FOR THE CONSTELLATIONS DATA

A summary of the algorithm is given in Algorithm 3.

Assume we have chosen parts n_1 and n_2 as the basis for object k , and that we have selected datapoints \mathbf{x}_i and \mathbf{x}_j as their hypothesized counterparts in the image. Let \mathbf{x}_{ij} be the vector obtained by stacking \mathbf{x}_i and \mathbf{x}_j , and B_k be the 4×4 square matrix obtained by stacking F_{kn_1} and F_{kn_2} . Then $\hat{\mathbf{y}}_k = B_k^{-1} \mathbf{x}_{ij}$. Finally, $\text{SubsetMatch}(\hat{X}_k, X)$ selects those points in X_k that are close to X with a given tolerance and add them to the output. Among them, the solution is given by the one that minimizes $\sum_{n=1}^{N_k} (\hat{x}_{nk} - x_{nk})^2$.

The above algorithm chooses a specific basis for each object, but one can consider all possible bases for each object. It is then efficient to use a hash table to store the predictions for each part, as used in Geometric Hashing [Wolfson and Rigoutsos, 1997]. Geometric Hashing is traditionally employed in computer vision to match geometric features against previously defined models of such features. This technique works well with partially occluded objects, and is computationally efficient if the basis dimension is low.

C EVALUATION METRICS FOR THE CONSTELLATIONS DATA

In a given scene X there are M points, but we know that there are $N \geq M$ possible points that can be produced from all of the templates. Assume that $K' \leq K$ templates are active in this scene. Then the points in the scene are

labelled with indices $1, \dots, K'$, and we assign the missing points index 0. Denote the ground truth partition as $V = \{V_0, V_1, \dots, V_{K'}\}$. An alternative partition output by one of the algorithms is denoted by $\hat{V} = \{\hat{V}_0, \hat{V}_1, \dots, \hat{V}_{K'}\}$. The predicted partition \hat{V} may instantiate objects or points that were in fact missing, thus it is important to handle the missing data properly.

In Information Theory, the **variation of information** (VI) [Meilă, 2003] is a measure of the distance between two partitions of elements (or clusterings). For a given set of elements, the variation of information between two partitions V and \hat{V} , where $N = \sum_i |V_i| = \sum_j |\hat{V}_j|$ is defined as:

$$VI(V, \hat{V}) = - \sum_{i,j} r_{ij} \left[\log \frac{r_{ij}}{p_i} + \log \frac{r_{ij}}{q_j} \right] \quad (26)$$

where $r_{ij} = \frac{|V_i \cap \hat{V}_j|}{N}$, $p_i = \frac{|V_i|}{N}$ and $q_j = \frac{|\hat{V}_j|}{N}$. In our experiments we report the average variation of information of the scenes in the dataset.

The **Rand index** [Rand, 1971] is another measure of similarity between two data clusterings. This metric takes pairs of elements and evaluates whether they do or do not belong to the same subsets in the partitions V and \hat{V}

$$RI = \frac{TP + TN}{TP + TN + FP + FN}, \quad (27)$$

where TP are the true positives, TN the true negatives, FP the false positives and FN the false negatives. The Rand index takes on values between 0 and 1. We use instead the **adjusted Rand index** (ARI) [Hubert and Arabie, 1985], the corrected-for-chance version of the Rand index. It uses the expected similarity of all pair-wise comparisons between clusterings specified by a random model as a baseline to correct for assignments produced by chance. Unlike the Rand index, the adjusted Rand index can return negative values if the index is less than the expected value. In our experiments, we compute the average adjusted Rand index of the scenes in our dataset.

The **segmentation accuracy** (SA) is based on obtaining the maximum bipartite matching between V and \hat{V} , and was used by Kosiorek et al. [2019] to evaluate the performance of CCAE. For each set V_i in V and set \hat{V}_j in \hat{V} , there is an edge w_{ij} with the weight being the number of common elements in both sets. Let $W(V, \hat{V})$ be the overall weight of the maximum matching between V and \hat{V} . Then we define the average segmentation accuracy as:

$$SA = \sum_{i=1}^I \frac{W(V_i, \hat{V}_i)}{W(V_i, V_i)} = \frac{1}{N} \sum_{i=1}^I W(V_i, \hat{V}_i), \quad (28)$$

where I is the number of scenes. Notice that $W(V_i, V_i)$ represents a perfect assignment of the ground truth, both the observed and missing subsets, and thus $W(V_i, V_i) = N$.

There are some differences on how we compute the SA metric compared to Kosiorek et al. [2019]. First, they do not consider the missing points as part of their ground truth, but as we argued above this is necessary. They evaluate the segmentation accuracy in terms of the observed points in the ground truth, disregarding possible points that were missing in the ground truth but predicted as observed in \hat{V} . Second, they average the segmentation accuracy across scenes as

$$SA = \frac{\sum_{i=1}^I W(V_i, \hat{V}_i)}{\sum_{i=1}^I W(V_i, V_i)}. \quad (29)$$

For them, $W(V_i, V_i) = M_i$, where M_i is the number of points present in a scene. In our case, both averaging formulae are equivalent since our $W(V_i, V_i)$ is the same across scenes.

D FAILURES OF ROTATION EQUIVARIANCE FOR SCAE

We trained the SCAE model with digit “4” images from the training set of the MNIST dataset⁶, after they had been uniformly rotated by up to 360° and uniformly translated by up to 6 pixels on the x and y axes. Since we used a single class in the dataset we altered SCAE’s architecture to use only a single object capsule.

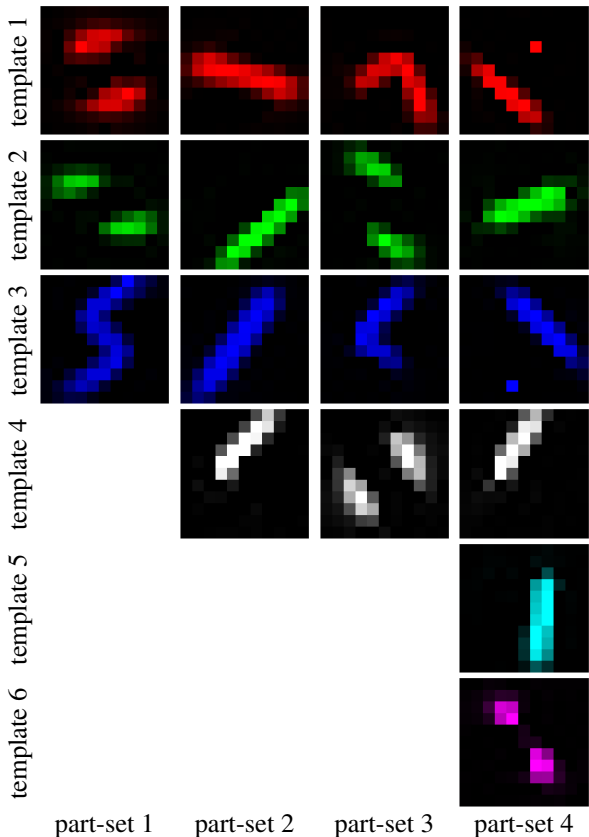
We repeated the training of SCAE multiple times for 8K epochs, and collected distinct sets of learned 11×11 parts that the digit “4” can be composed into (see Fig. 3). Afterwards, we evaluated PCAE’s ability to detect these parts in MNIST digit “4” images that had been rotated by multiples of 45° . Then, we measured the average inferred pose of each part at each of the different angles of rotations. Our results indicate that the PCAE model is not equivariant to rotations. This is apparent from Fig. 7, where the learned parts from part-sets 2 and 3 of Fig. 3 are inconsistently assigned to the regions of the digit-object, depending on the angle of rotation. We hypothesize that this phenomenon stems from the fact that PCAE seems to generate either parts that are characterized by an intrinsic symmetry –and thus their pose is ambiguous– (e.g. template 3 of column (a) in Fig. 3) or pairs of parts that are transformed versions of themselves, and thus can be used interchangeably (e.g. templates 1 and 3 of part-set 3 in Fig. 3). This leads to identifiability issues, where the object can be decomposed into its parts in numerous ways.

E DIFFERENT INITIALIZATIONS OF β

In this section, we show the effect of varying the initial value of β for the variational inference method with a Gaussian mixture prior (8) (GCM-GMM) and with a prior over

⁶<http://yann.lecun.com/exdb/mnist>.

Figure 3: Each column corresponds to a part-set of learned templates parts of size 3, 4, 4 and 6 respectively.



permutation matrices (9) (GCM-DS). We have tested 6 different values of β : 0.005, 0.01, 0.05, 0.1, 0.2, 0.5. In Tables 2, 3 and 4 we show the results for all metrics, methods and initial values of β for $\sigma = 0$, $\sigma = 0.1$, and $\sigma = 0.25$ resp.

We can observe that no matter the initialization of β , GCM-DS is always better than CCAE and GCM-GMM. As we increase the initial β , GCM-DS performs better across all the metrics. We have found that the performance of GCM-DS and GCM-GMM degrades with $\beta > 0.1$.

We have conducted paired t-tests between CCAE and GCM-GMM, GCM-DS and RANSAC on the three clustering metrics for $\sigma = 0$ and initial $\beta = 0.05$. The differences between CCAE and GCM-DS are statistically significant with p-values less than 10^{-7} , and between CCAE and RANSAC with p-values less than 10^{-28} . For CCAE and GCM-GMM the differences are not statistically significant.

Table 2: Different initializations of β . For SA, ARI and Scene Accuracy the higher the better. For VI the lower the better. Noise-free case.

Model	SA \uparrow	ARI \uparrow	VI \downarrow	Sc. Acc. \uparrow
CCAe	0.828	0.599	0.481	0.365
GCM-DS $\beta = 0.005$	0.869	0.667	0.350	0.581
GCM-DS $\beta = 0.01$	0.876	0.678	0.328	0.624
GCM-DS $\beta = 0.05$	0.899	0.740	0.299	0.664
GCM-DS $\beta = 0.1$	0.904	0.752	0.302	0.653
GCM-DS $\beta = 0.2$	0.899	0.728	0.332	0.622
GCM-DS $\beta = 0.5$	0.886	0.679	0.402	0.576
GCM-GMM $\beta = 0.005$	0.823	0.449	0.592	0.402
GCM-GMM $\beta = 0.01$	0.823	0.487	0.555	0.362
GCM-GMM $\beta = 0.05$	0.753	0.586	0.478	0.179
GCM-GMM $\beta = 0.1$	0.771	0.550	0.543	0.214
GCM-GMM $\beta = 0.2$	0.764	0.513	0.613	0.199
GCM-GMM $\beta = 0.5$	0.762	0.488	0.650	0.194

Table 3: Different initializations of β . For SA, ARI and Scene Accuracy the higher the better. For VI the lower the better. Gaussian noise with $\sigma = 0.1$.

Model	SA \uparrow	ARI \uparrow	VI \downarrow	Sc. Acc. \uparrow
CCAe	0.754	0.484	0.689	0.138
GCM-DS $\beta = 0.005$	0.840	0.608	0.451	0.518
GCM-DS $\beta = 0.01$	0.859	0.644	0.389	0.559
GCM-DS $\beta = 0.05$	0.883	0.699	0.359	0.603
GCM-DS $\beta = 0.1$	0.888	0.715	0.352	0.601
GCM-DS $\beta = 0.2$	0.874	0.682	0.406	0.544
GCM-DS $\beta = 0.5$	0.872	0.659	0.443	0.515
GCM-GMM $\beta = 0.005$	0.793	0.468	0.566	0.322
GCM-GMM $\beta = 0.01$	0.800	0.497	0.547	0.318
GCM-GMM $\beta = 0.05$	0.757	0.573	0.502	0.173
GCM-GMM $\beta = 0.1$	0.768	0.521	0.595	0.204
GCM-GMM $\beta = 0.2$	0.765	0.460	0.684	0.178
GCM-GMM $\beta = 0.5$	0.753	0.403	0.780	0.140

F COMPARISON ACROSS METHODS USING THE GROUND TRUTH MISSING INDICATORS

. The results above include the missing objects in the creation of \hat{V} , as described in supp. mat. C. Failing to recognize exactly which points in a scene are missing leads to a decrease in performance for all the metrics. However, Kosiorek et al. [2019] instead used the ground truth missing indicators for the objects in order to compute the segmentation accuracy of their method (see equation 29) If we use this strategy to all the models and metrics, we obtain Tables 5, 6 and 7. When we compare these results with the tables in the previous section we can see that this alternative leads to a clear improvement in the scores of all the methods, but with GCM-DS still performing better than CCAE or GCM-GMM.

Table 4: Different initializations of β . For SA, ARI and Scene Accuracy the higher the better. For VI the lower the better. Gaussian noise with $\sigma = 0.25$.

Model	SA \uparrow	ARI \uparrow	VI \downarrow	Sc. Acc. \uparrow
CCAЕ	0.623	0.248	0.988	0.033
GCM-DS $\beta = 0.005$	0.771	0.475	0.669	0.338
GCM-DS $\beta = 0.01$	0.781	0.486	0.652	0.362
GCM-DS $\beta = 0.05$	0.785	0.498	0.659	0.377
GCM-DS $\beta = 0.1$	0.779	0.476	0.699	0.351
GCM-DS $\beta = 0.2$	0.768	0.470	0.708	0.291
GCM-DS $\beta = 0.5$	0.766	0.435	0.752	0.272
GCM-GMM $\beta = 0.005$	0.736	0.469	0.564	0.265
GCM-GMM $\beta = 0.01$	0.730	0.467	0.581	0.221
GCM-GMM $\beta = 0.05$	0.744	0.447	0.677	0.132
GCM-GMM $\beta = 0.1$	0.735	0.387	0.801	0.102
GCM-GMM $\beta = 0.2$	0.727	0.310	0.921	0.088
GCM-GMM $\beta = 0.5$	0.717	0.242	1.036	0.064

Table 5: Different initializations of β using the ground truth missing mask. For SA, ARI and Scene Accuracy the higher the better. For VI the lower the better. Noise-free case.

Model	SA \uparrow	ARI \uparrow	VI \downarrow	Sc. Acc. \uparrow
CCAЕ	0.950	0.897	0.157	0.736
GCM-DS $\beta = 0.005$	0.985	0.967	0.052	0.915
GCM-DS $\beta = 0.01$	0.989	0.973	0.042	0.941
GCM-DS $\beta = 0.05$	0.971	0.938	0.095	0.886
GCM-DS $\beta = 0.1$	0.966	0.929	0.108	0.860
GCM-DS $\beta = 0.2$	0.966	0.930	0.104	0.854
GCM-DS $\beta = 0.5$	0.958	0.912	0.132	0.825
GCM-GMM $\beta = 0.005$	0.886	0.805	0.209	0.646
GCM-GMM $\beta = 0.01$	0.905	0.830	0.191	0.683
GCM-GMM $\beta = 0.05$	0.942	0.884	0.160	0.718
GCM-GMM $\beta = 0.1$	0.937	0.879	0.179	0.657
GCM-GMM $\beta = 0.2$	0.927	0.861	0.213	0.603
GCM-GMM $\beta = 0.5$	0.925	0.858	0.216	0.585

G EXAMPLES OF CCAE AND GCM-DS INFERENCE FOR THE CONSTELLATIONS DATA

Figure 4 shows some reconstruction examples from CCAE and GCM-DS for the noise-free scenario. We show additional examples for the noisy cases in the supp. mat. H. In columns (a) and (b) we can see that CCAE recovers the correct parts assignments but the object reconstruction is amiss. In (a) one of the squares is reconstructed as a triangle, while in (b) the assignment between the reconstruction and the ground truth is not exact. For GCM-DS, if the parts are assigned to the ground truth properly, and there is no noise, then the reconstruction of the object is perfect. In column (c) all methods work well. In column (d), CCAE fits the square correctly (green), but adds an additional red point. In this case GCM-DS actually overlays two squares on top of each other. Both methods fail badly on column (e). Note that CCAE is not guaranteed to reconstruct an existing object

Table 6: Different initializations of β using the ground truth missing mask. For SA, ARI and Scene Accuracy the higher the better. For VI the lower the better. Gaussian noise with $\sigma = 0.1$

Model	SA \uparrow	ARI \uparrow	VI \downarrow	Sc. Acc. \uparrow
CCAЕ	0.867	0.729	0.403	0.386
GCM-DS $\beta = 0.005$	0.957	0.917	0.135	0.794
GCM-DS $\beta = 0.01$	0.972	0.940	0.094	0.857
GCM-DS $\beta = 0.05$	0.957	0.908	0.142	0.833
GCM-DS $\beta = 0.1$	0.956	0.906	0.144	0.831
GCM-DS $\beta = 0.2$	0.946	0.887	0.172	0.794
GCM-DS $\beta = 0.5$	0.942	0.875	0.194	0.759
GCM-GMM $\beta = 0.005$	0.856	0.752	0.272	0.544
GCM-GMM $\beta = 0.01$	0.875	0.768	0.272	0.561
GCM-GMM $\beta = 0.05$	0.922	0.837	0.232	0.621
GCM-GMM $\beta = 0.1$	0.912	0.824	0.268	0.548
GCM-GMM $\beta = 0.2$	0.905	0.822	0.278	0.474
GCM-GMM $\beta = 0.5$	0.881	0.792	0.334	0.379

Table 7: Different initializations of β using the ground truth missing mask. For SA, ARI and Scene Accuracy the higher the better. For VI the lower the better. Gaussian noise with $\sigma = 0.25$

Model	SA \uparrow	ARI \uparrow	VI \downarrow	Sc. Acc. \uparrow
CCAЕ	0.774	0.621	0.540	0.033
GCM-DS $\beta = 0.005$	0.897	0.811	0.302	0.556
GCM-DS $\beta = 0.01$	0.908	0.822	0.281	0.611
GCM-DS $\beta = 0.05$	0.900	0.805	0.302	0.623
GCM-DS $\beta = 0.1$	0.895	0.796	0.317	0.609
GCM-DS $\beta = 0.2$	0.891	0.784	0.333	0.578
GCM-DS $\beta = 0.5$	0.881	0.770	0.359	0.528
GCM-GMM $\beta = 0.005$	0.852	0.743	0.287	0.545
GCM-GMM $\beta = 0.01$	0.865	0.756	0.282	0.558
GCM-GMM $\beta = 0.05$	0.887	0.773	0.337	0.468
GCM-GMM $\beta = 0.1$	0.869	0.748	0.392	0.355
GCM-GMM $\beta = 0.2$	0.855	0.734	0.419	0.278
GCM-GMM $\beta = 0.5$	0.834	0.704	0.470	0.196

correctly (square or triangle in this case). In column (f) we can see that CCAE fits an irregular quadrilateral (blue) to the assigned points, while GCM-DS obtains the correct fit.

H NOISY CASES EXAMPLES

In Figures 5 and 6 we show several examples of objects generated from noisy templates with corruption levels of $\sigma = 0.1$ and $\sigma = 0.25$ resp. GCM-DS and RANSAC does not allow for deformable objects to try to fit the points exactly, contrary to CCAE. Both methods try to find the closest reconstruction of the noisy points in the image by selecting the geometrical shapes that are a best fit to those points. Nonetheless, both methods can determine that which parts belong together to form a given object, even when the matching is not perfect.

Figure 4: Reconstruction examples from CCAE and GCM-DS for noise-free data. The upper figures show the ground truth of the test images. The middle figures show the reconstruction and the capsule assignments (by colours) of CCAE. The lower figures show the reconstruction and the parts assignment of GCM-DS. Datapoints shown with a given colour are predicted to belong to the reconstructed object with the corresponding colour.

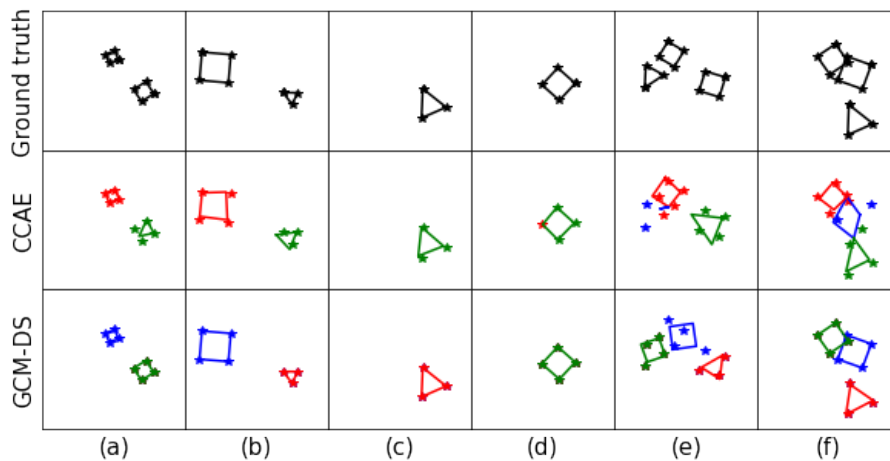


Figure 5: Reconstruction examples from CCAE, GCM-DS and RANSAC with Gaussian noise $\sigma = 0.1$.

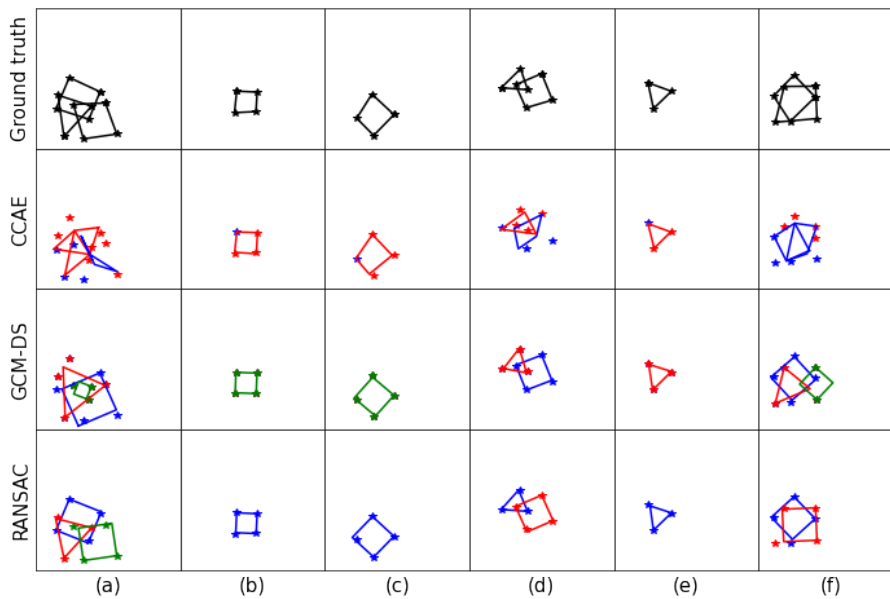


Figure 6: Reconstruction examples from CCAE, GCM-DS and RANSAC with Gaussian noise $\sigma = 0.25$.

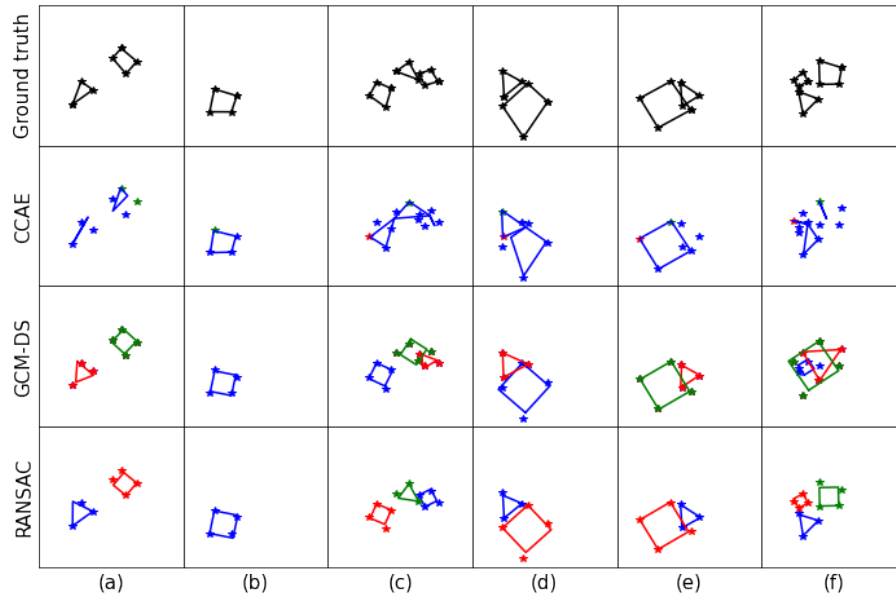


Figure 7: Average part-based reconstruction for different angles of rotation of the input scenes. Row (a) corresponds to reconstructions with the learned part-sets 2 and row (b) reconstructions with the learned part-sets 3 of Fig. 3.

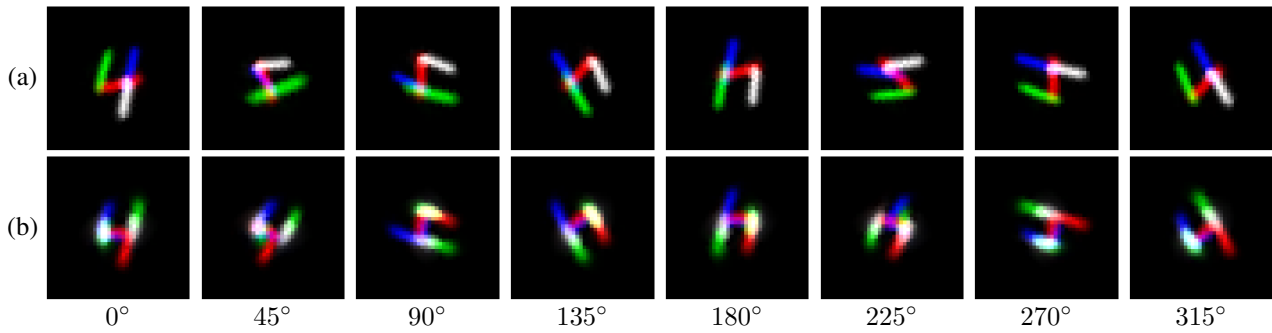


Figure 8: Reconstruction examples with our Variational Inference (VI) algorithm and the RANSAC-type algorithm: (a) scene with 2 faces, (b) scene with 3 faces, (c) scene with 4 faces (d) scene with 5 faces and (e) 3 faces with partially occluded faces. All faces have been randomly selected and transformed.

